

Non-convex Quadratic Programming Using Coherent Optical Networks

Farhad Khosravi,¹ Ugur Yildiz,¹ Artur Scherer,¹ and Pooya Ronagh^{1, 2, 3, 4, *}

¹*1QB Information Technologies (1QBit), Vancouver, BC, Canada*

²*Institute for Quantum Computing, University of Waterloo, Waterloo, ON, Canada*

³*Department of Physics & Astronomy, University of Waterloo, Waterloo, ON, Canada*

⁴*Perimeter Institute for Theoretical Physics, Waterloo, ON, Canada*

(Dated: September 20, 2022)

We investigate the possibility of solving continuous non-convex optimization problems using a network of interacting quantum optical oscillators. We propose a native encoding of continuous variables in analog signals associated with the quadrature operators of a set of quantum optical modes. Optical coupling of the modes and noise introduced by vacuum fluctuations from external reservoirs or by weak measurements of the modes are used to optically simulate a diffusion process on a set of continuous random variables. The process is run sufficiently long for it to relax into the steady state of an energy potential defined on a continuous domain. As a first demonstration, we numerically benchmark solving box-constrained quadratic programming (BoxQP) problems using these settings. We consider delay-line and measurement-feedback variants of the experiment. Our benchmarking results demonstrate that in both cases the optical network is capable of solving BoxQP problems over three orders of magnitude faster than a state-of-the-art classical heuristic.

I. INTRODUCTION

Real-world optimization problems frequently involve decision variables that are naturally continuous. This is the case for continuous non-convex global optimization problems and the more general class of mixed-integer programming (MIP) models [1] designed to solve a variety of NP-hard optimization problems of high practical relevance, including, for example, scheduling problems, flow problems, resource allocation problems, and routing problems. Even the special class of quadratic non-convex global optimization problems captures extremely challenging computational tasks that are NP-hard [2, 3]. Classical optimization techniques lack satisfactory performance in solving continuous non-convex optimization problems at scale [3–5].

In recent years, the design of special-purpose computing architectures for solving optimization problems has been gaining increasing attention [6]. Common discrete optimization engines include physics-inspired heuristics such as thermal (simulated) annealing [7, 8] and its variants [9, 10], quantum annealing [11–14], coherent Ising machines (CIM) [15, 16], local heuristic search techniques [17, 18], and various spin-based Monte Carlo methods. All these approaches focus on solving discrete optimization problems natively, and even in that class, the attention has been limited to solving Ising problems. This means that more-general types of problems (e.g., those comprising continuous variables) require processing at the software level. Algorithmic problem reformulation and reduction is not only costly in terms of the computing resources it requires, but it can result in ill-behaved energy landscapes that are difficult to optimize. Such

schemes hinder the practical applicability of the resultant technologies, as evidenced by over a decade’s worth of unsuccessful attempts to find practical applications for the technologies.

As demonstrated by several previous studies [19–23], coherent-network computing has appeared as a promising approach for solving NP-hard combinatorial optimization problems. The well-known CIM utilizes a network of degenerate optical parametric oscillators (degenerate OPO or DOPO) that are injected into a ring cavity and gradually pumped at a rate well above the bifurcation threshold [15, 16]. The CIM can be realized as either a fully optical experiment involving optical delay lines [24, 25], abbreviated as DL-CIM, or using the assistance of a digital processing device (e.g., an FPGA) in a measurement-feedback procedure [20, 26], abbreviated as MF-CIM. While the digital processor may limit the performance of the measurement-feedback variant, in principle, by operating at optical frequencies, the CIM operates at a much faster clock speed and far lower power consumption compared to digital computers. With optical pulses that are only a few picoseconds apart, the CIM can solve binary optimization problems involving thousands of variables in a fraction of a second [27].

Pumping DOPOs above their bifurcation threshold forces their amplitudes to attain certain extreme positive or negative values. In this paper, we show that if the DOPOs are pumped less aggressively, their mean-field amplitudes can converge to stable fractional values. When solving binary optimization problems, the conventional CIM begins an optimization process as a quantum analog device and finishes it as a classical digital device [28]. This quantum-to-classical and analog-to-digital transition is a key characteristic of the CIM. However, being intrinsically continuous, the analog amplitudes of the DOPO pulses can be used to represent continuous variables of a continuous optimization problem below the bifurcation threshold. In order to encourage the realiza-

* Corresponding author: pooya.ronagh@1qbit.com

tion of experiments beyond Ising optimization, we refer to our setup as a coherent continuous-variable machine (CCVM).

At the pump rates at which a CCVM is operated, the entire time evolution is carried out in the coherent regime of the device. While this itself opens the door to investigating the signatures of a quantum parallel search, we do not focus on such aspects of the operation of the machine, and instead view the machine as an optical device intended to *optically* perform a Brownian motion process which is then used to *optically* integrate a diffusion process of the form

$$dc = b(t, c) dt - \nabla f(c) dt + \sigma(t) dW. \quad (1)$$

Here, c represents the mean amplitude and phase of the DOPOs, f is a continuous function we are interested in minimizing, and $b(t, c)$ is a component-wise force driving the dynamics of each DOPO, which are controlled by the DOPO's pump rate. The variable W is a standard Wiener process realized by weak measurements of the optical modes either via photon loss in a highly dissipative cavity, particularly in a delay-line CCVM (DL-CCVM), or via out-coupling and homodyne detection in a measurement-feedback CCVM (MF-CCVM). Finally, $\sigma(t)$ represents the diffusion rate, and is controlled via the usage of cavities with a certain amount of finesse in the DL-CCVM, or by controlling the out-coupling rate of beamsplitters in the MF-CCVM.

Monte Carlo simulations of such stochastic differential equations (SDE) have provided a breath of techniques in digital computing for solving global optimization problems [29, 30]. Indeed, the convergence rate of diffusion processes of the form presented above are well-studied. For instance, if the drift is a conservative force satisfying Poincaré or log-Sobolov inequalities, then the process mixes exponentially fast in the Gibbs distribution of the potential, but for highly non-convex potentials the mixing time is exponentially long. We do not propose employing coherent computing as a way to avoid exponentially long mixing times. Instead, we are interested in proposing power-efficient computing architectures that *naturally* integrate SDEs of the form given above by exploiting the quantum mechanical properties of light.

Our long-term goal is to explore the capabilities of CCVMs in solving continuous and mixed-integer non-convex optimization problems natively, thereby avoiding the aforementioned overhead. As a first step, we benchmark the performance of our proposed technology by predicting the time-to-solution (TTS) scaling of CCVMs for solving a simple example of continuous non-convex optimization problems, that is, the *box-constrained quadratic programming* (BoxQP) problem [31]. This is the simplest non-convex optimization problem one can attempt to solve, yet it is NP-hard [32] and no reasonably efficient classical algorithms for solving it exist [3–5].

This paper is organized as follows. In Section II, we introduce the various SDEs used to solve the BoxQP problem in our benchmarking study, including the systems

of SDEs that represent the dynamics of the DL-CCVM and the MF-CCVMs. In Section III, we propose methods by which these algorithms for solving BoxQP problems can be experimentally realized. Our benchmarking results are presented in Section IV. In Section V, we analyze the time evolution of the optical pulses in the DL-CCVM scheme when solving BoxQP problems. We conclude with a brief discussion and prospects for future research in Section VI.

II. SDEs GOVERNING CCVM DYNAMICS

Let $f: \mathbb{R}^N \rightarrow \mathbb{R}$ be a real-valued differentiable function of N variables. To explore the dynamics of the proposed CCVM as a heuristic for the global optimization of f , we consider six systems of SDEs. The first system of SDEs is the typical *Langevin dynamics*, the convergence properties of which have been well-studied in mathematics and computer science [33]:

$$dc_i = -\partial_i f(c) dt + \sigma dW_i \quad \forall i \in \{1, \dots, N\}. \quad (2)$$

Here, c_i are N continuous random variables, and $dW_i \sim \sqrt{dt} N(0, 1)$, hence injecting Gaussian noise of with a mean of zero and variance of dt into the dynamics. We use ∂_i to denote the i -th partial derivative $\partial_i = \partial/\partial c_i$. For example, if $f(c) = \sum_{i,j=1, \dots, N} \xi_{ij} c_i c_j$ is a quadratic function, then the i -th drift term is $-\partial_i f(c) = -\sum_{j=1}^N \xi_{ij} c_j$, which may be realized physically via two-mode interactions.

The second system of SDEs is a modification of Langevin dynamics of the form

$$dc_i = (-1 + p - c_i^2) c_i dt - \partial_i f(c) dt + \sigma dW_i. \quad (3)$$

Here, the equation of motion [Eq. (2)] is augmented with an additional drift term representing three physical processes: the constant -1 represents a photon loss rate that is normalized to that of the optical cavity; the parameter p represents the strength of the external pump field (e.g., a laser), normalized to the photon decay rate at the signal frequency γ_s , inducing an amplification of field strengths in the cavity during the process; and the term c_i^2 results from the nonlinear self-interaction induced by a nonlinear crystal (e.g., a periodically poled lithium niobate crystal (PPLN)) [15]. We refer to this system of SDEs as *pumped Langevin dynamics*.

The third system of SDEs is akin to the continuous-time model for the optical DL-CIM [24, 25], a fully quantum model for describing the trajectories of the amplitudes of the DOPO pulses inside the cavity via the positive P-representation expressed in terms of pairs of the random variables c_i and s_i representing the in-phase and

quadrature-phase components of the signal field [34]

$$\begin{aligned} dc_i &= [(-1 + p - c_i^2 - s_i^2) c_i - \partial_i f(c)] dt \\ &\quad + \frac{1}{A_s} \sqrt{c_i^2 + s_i^2 + \frac{1}{2}} dW_{i1}, \\ ds_i &= [(-1 - p - c_i^2 - s_i^2) s_i - \partial_i f(c)] dt \\ &\quad + \frac{1}{A_s} \sqrt{c_i^2 + s_i^2 + \frac{1}{2}} dW_{i2}, \end{aligned} \quad (4)$$

where the Wiener increments dW_{i1} and dW_{i2} are independently sampled from an identical distribution. Here, $A_s = (\gamma_p \gamma_s / 2\kappa^2)^{1/2}$, with γ_s and γ_p being the signal and pump decay rates, respectively. The parameter κ represents the parametric gain due to the second-order susceptibility of the nonlinear crystal.

We note that the drift term in Eq. (4) may not be realizable for arbitrary differentiable functions f . Even in the case of polynomials, this requires the experimental realization of higher-order optical interactions, which is a challenge being tackled in current research [35]. Therefore, we restrict our study to the case of quadratic functions, as two-mode interactions of programmable strength can be realized using optical delay lines and beamsplitters. With this in mind, we refer to the system of SDEs (4) as *DL-CCVM dynamics*.

The final three systems of SDEs studied follow the continuous-time model of the MF-CIM [20, 26]. For the conventional MF-CIM, under the assumption that the DOPO pulses maintain a Gaussian distribution throughout the time evolution, their mean values and variances, μ_i and σ_i , follow the SDEs [36],

$$\begin{aligned} d\mu_i &= [-(1 + j) + p - g^2 \mu_i^2] \mu_i dt \\ &\quad - \lambda \partial_i f(\tilde{\mu}) dt + \sqrt{j}(\sigma_i - 1/2) dW_i, \\ d\sigma_i &= 2 [-(1 + j) + p - 3g^2 \mu_i^2] \sigma_i dt \\ &\quad - 2j(\sigma_i - 1/2)^2 dt + [(1 + j) + 2g^2 \mu_i^2] dt, \end{aligned} \quad (5)$$

where j is the normalized continuous measurement strength, λ is a hyperparameter, and g is the normalized second-order nonlinearity coefficient. We refer to this system of SDEs as *MF-CCVM dynamics*. An alternative measurement-feedback scheme can be obtained by removing the nonlinear crystal and the external pump field, which is governed by a simpler system of SDEs:

$$\begin{aligned} d\mu_i &= -(1 + j)\mu_i dt - \lambda \partial_i f(\tilde{\mu}) dt + \sqrt{j}(\sigma_i - 1/2) dW_i, \\ d\sigma_i &= -2(1 + j)\sigma_i dt - 2j(\sigma_i - 1/2)^2 dt + [(1 + j)] dt. \end{aligned} \quad (6)$$

We refer to this system of SDEs, which represents a bare form of MF-CCVM, as *BMF-CCVM dynamics*. This equation eliminates the contributions of the pump and saturation terms from the drift of the SDEs. Furthermore, by tuning the pump for each optical pulse individually we may correct the deviation of the drift term from

the negative gradient flow of f even further:

$$\begin{aligned} d\mu_i &= -(1 + j)\mu_i dt \\ &\quad + [(1 + j)\tilde{\mu}_i - \lambda \partial_i f(\tilde{\mu})] dt + \sqrt{j}(\sigma_i - 1/2) dW_i, \\ d\sigma_i &= -2(1 + j)\sigma_i dt \\ &\quad - 2j(\sigma_i - 1/2)^2 dt + [(1 + j)] dt. \end{aligned} \quad (7)$$

Here, a pulse with an amplitude of $p_i = (1 + j)\tilde{\mu}_i$ is injected back into the cavity after a homodyne measurement is performed in order to approximately cancel out the drift of value $(1 + j)\mu_i$. We refer to this system of SDEs, which represents a pumped form of BMF-CCVM, as *PMF-CCVM dynamics*.

Note that, unlike in the previous systems of SDEs, the gradient field of f in the above three variants of the MF-CCVM, defined by Eqs. (5) to (7), is evaluated at a measured mean-field amplitude vector $\tilde{\mu}$ which differs from the instantaneous mean-field amplitude within the cavity by a random vector representative of the uncertainty of the continuous quantum measurements:

$$\tilde{\mu} = \mu + \sqrt{\frac{1}{4j}} \frac{dW}{dt}. \quad (8)$$

It is also important to note that these schemes can be realized for arbitrary differentiable functions f , since the feedback term $-j\partial_i f(\tilde{\mu})$ is calculated via a digital processor, for example, an FPGA, GPU, an application-specific integrated circuit (ASIC), or perhaps via on-chip photonics.

Whereas Langevin and pumped Langevin dynamics serve as heuristic algorithms to be implemented on standard classical hardware via Monte Carlo simulations, the DL-CCVM and the three variants of the MF-CCVM are investigated as solvers that can be implemented on both standard digital hardware and analog quantum-optical devices. In our simulations, the success probabilities of these solvers are used to predict the wall-clock TTS of the respective physical machines. The wall-clock TTS is computed from the round-trip time of the optical pulses in the cavity, the pulse durations, and the number of pulses; for more details, see Section IV.

III. SOLVING BoxQP PROBLEMS

The BoxQP problem can be formulated as follows:

$$\begin{aligned} \text{maximize } \quad f(x) &= \sum_{i,j=1}^N Q_{ij} x_i x_j + \sum_{i=1}^N V_i x_i, \\ \text{subject to } \quad \ell_i &\leq x_i \leq u_i \quad \forall i \in \{1, \dots, N\}, \end{aligned} \quad (9)$$

where $Q \in \mathbb{R}^{N \times N}$ is a symmetric matrix, $V \in \mathbb{R}^N$ is a real N -dimensional vector, and the lower and upper bounds $\ell_i \in \mathbb{R}$ and $u_i \in \mathbb{R}$ specify the box constraints.

In both the DL-CIM and MF-CIM, a nonlinear crystal placed in an optical ring cavity fed by a sequence of pump laser pulses plays a key role. A PPLN crystal is commonly used to generate a degenerate nonlinear optical parametric process: some pump photons with a frequency of ω_p are down-converted to two degenerate signal photons that have the frequency $\omega_s = 0.5\omega_p$. These signal photon pulses then propagate inside the optical ring cavity loop, and are coherently amplified in each roundtrip by passing through the PPLN crystal. In our proposal, the nonlinear crystal is not essential for a measurement-feedback scheme and therefore we benchmark three approaches: MF-CCVM, which incorporates a PPLN crystal and the pump as in the standard MF-CIM shown in Eq. (5); BMF-CCVM, which excludes both a PPLN crystal and a pump as shown in Eq. (6); and PMF-CCVM, which excludes a PPLN crystal but includes an external laser source as shown in Eq. (7). We note that, in the DL-CCVM, the nonlinear crystal continues to play an important role as it is the only active element in the system and amplifies the vacuum state toward coherent states representative of the solution. We also note that, in both the BMF-CCVM and the PMF-CCVM, the quantum information is stored in the coherent states of optical pulses but no DOPOs are utilized.

In CIMs, the pump rate of DOPOs is increased from below a bifurcation threshold to a pump rate above the threshold. This creates a transition from squeezed vacuum states below the threshold to coherent states with a binary phase oscillation (0 or π). Meanwhile, the pulse amplitudes saturate to extreme minimum and maximum values that depend on the properties of the nonlinear crystal and the pump field strength [15]. Operating in this regime allows a CIM to solve binary optimization problems. In contrast, we are interested in performing the same experiment below the bifurcation threshold, where instead of a binary spin, we obtain an analog degree of freedom encoded in the linear superposition of quadrature amplitude eigenstates forming the squeezed vacuum state.

During each roundtrip, a portion of each optical pulse is coupled out of the optical ring cavity to calculate and re-inject the drift term $-\nabla f$. In all variants of the MF-CCVM, each out-coupled pulse is measured using a homodyne measurement. This measurement serves two key roles: it creates the Brownian motion $\sqrt{j}(\sigma_i - 1/2)dW_i$ as required for the diffusion process; and it provides the measured mean-field amplitudes $\tilde{\mu}$, which are then converted to digital information and used to compute $-\nabla f(\tilde{\mu})$ via a digital processor. The result is then converted back to an analog signal. Intensity and phase modulators clock-locked with the external pump are used to achieve amplitudes equal to the partial derivatives $\partial_i f(\tilde{\mu})$, and to match the phase of the newly generated pulses with that of the original pulse. The result is injected back into the main optical ring cavity at the appropriate time for each optical pulse [27].

In contrast, in the DL-CCVM scheme, the drift terms

$-\partial_i f(c) = \sum_{j=1}^N \xi_{ij} c_j$ are linear functions of pulse amplitudes. As with the DL-CIM, this coupling term may be calculated through a network of delay lines. Each pulse is split between optical lines of different lengths using an array of beam splitters. The amplitude and the phase of the pulses within each delay line are appropriately manipulated using amplitude and phase modulators, before the pulses join back together to create a coupling term. The roundtrip time for both architectures can be estimated as the pulse repetition time multiplied by the number of pulses [25, 27].

The continuous variables of the BoxQP problem can be natively encoded into analog pulse amplitudes. The box constraints can be implemented either by exploiting the saturation thresholds of the pulse amplitudes in the case of the DL-CCVM and the MF-CCVMs, described by Eq. (4) and Eq. (5), respectively, or, in all three variants of the MF-CCVM, Eqs. (5) to (7), by clipping the amplitudes during each roundtrip using the digital processor. Similarly, for the Langevin and pumped Langevin dynamics, the box constraints can be implemented by simply clamping each amplitude c_i between the respective lower and upper bounds ℓ_i and u_i at each iteration of Monte Carlo simulation.

More specifically, in the DL-CCVM scheme, by performing the change of variables

$$x_i \mapsto \frac{1}{2} \left(\frac{c_i}{s} + 1 \right) (u_i - \ell_i) + \ell_i, \quad (10)$$

we can enforce the box constraint for each DOPO pulse. Here, s is the saturation amplitude for all DOPO pulses, assuming that they all saturate to the same value. Therefore, the drift terms in the SDEs of the DL-CCVM described by Eq. (4) are

$$\begin{aligned} \partial_i f(c) = & \sum_{j=1}^N Q_{ij} \frac{u_i - \ell_i}{s} \left[\frac{1}{2} \left(\frac{c_j}{s} + 1 \right) (u_j - \ell_j) + \ell_j \right] \\ & + \frac{V_i(u_i - \ell_i)}{2s}, \end{aligned} \quad (11)$$

where we have substituted the variables in Eq. (9) by the expression on the right-hand side of Eq. (10) and taken the gradient of the objective function with respect to c_i . This expression is linear in the pulse amplitudes c_j and thus able to be implemented using the DL-CCVM. The coefficients of the pulse amplitudes in the above equation are equal to $-Q_{ij} \frac{(u_i - \ell_i)(u_j - \ell_j)}{2s^2}$. They can be implemented using the intensity and phase modulators on each delay line and for each pulse index j . The rest of the terms in Eq. (11) amount to the constant $\sum_j Q_{ij} \frac{(u_i - \ell_i)(u_j + \ell_j)}{2s} + \frac{V_i(u_i - \ell_i)}{2s}$, which can be calculated in advance and added to each pulse during each roundtrip. An offset value for each pulse can be introduced by an external source (e.g., a laser) that operates at the frequency of the optical DOPO pulses.

In the three MF-CCVM variants, the BoxQP problem's variables may simply be encoded as $x_i := \tilde{\mu}_i$. However, if the lower bounds ℓ_i are non-negative, which is

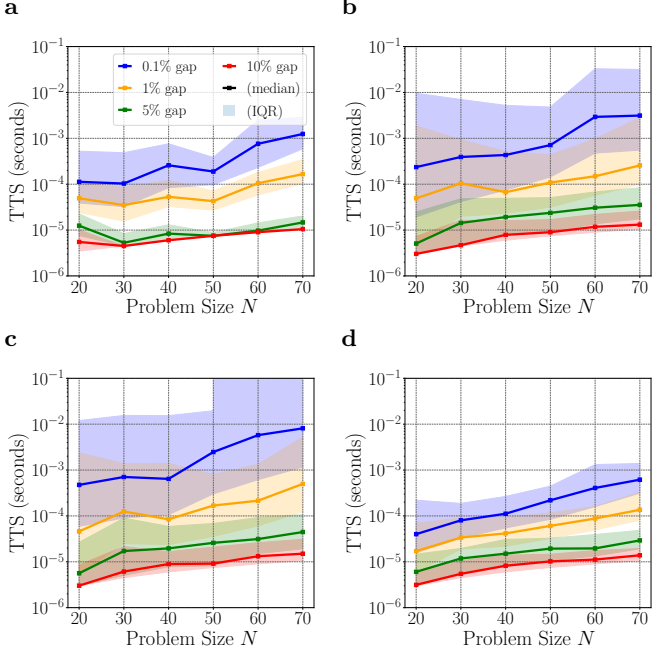


FIG. 1: Estimated physical TTS for various CCVM architectures. (a) DL-CCVM; (b) MF-CCVM; (c) BMF-CCVM; (d) PMF-CCVM. For each CCVM architecture, several TTS curves are displayed, corresponding to a solution within a certain target percentage gap from the optimal solution. The shaded regions show the IQR corresponding to the percentile of the solved instances that were found to be within the specified gap. For the BMF-CCVM plots in panel (c), the 75th percentile's edge of the IQR for the 0.1% gap goes to infinity for the problems of size 60 and 70, meaning that, for fewer than 75% of the instances, solutions were found to be within the 0.1% gap.

the case for the problems studied in Section IV, we use the encoding

$$x_i \mapsto \tilde{\mu}_i^2 \quad (12)$$

to increase the success probability of the optimizer. This encoding results in the following drift term:

$$\partial_i f(\tilde{\mu}) = 2 \sum_{k=1}^N Q_{ik} \tilde{\mu}_i \tilde{\mu}_k^2 + 2V_i \tilde{\mu}_i. \quad (13)$$

Note that such drift terms are no longer linear and therefore difficult to realize optically. However, because the feedback pulse is generated via a digital processor, any arbitrary mathematical function of input variables can be realized.

IV. BENCHMARKING RESULTS

We have tested the solvers introduced in the previous sections on randomly generated problem instances. We generated our instances using the same approach as in Ref. [37], where the elements of the $N \times N$ symmetric matrix Q and the vector V are random integers generated uniformly between -50 and $+50$. The generated instances are labelled N - D - S , where N is the problem

size, D is the density of the nonzero entries of Q and V , and S is the seed number of the random number generator. For simplicity, all variables are assumed to be constrained to the domain $[0, 1]$, that is, $\ell_i = 0$ and $u_i = 1$ for all $i \in \{1, \dots, N\}$. The global maxima of the generated instances were found using Gurobi 9.5 [38].

Figure 1 shows the physical TTS for the four CCVM architectures introduced in Section II. The TTS is defined as the number of trials that must be performed to ensure a high probability (specified by some target probability of success) of observing an optimal or an acceptable approximate solution at least once, multiplied by the time required for the execution of a single trial. Here, we assume a target probability of success of 0.99. Thus, we compute the TTS according to the equation $TTS = R_{99} \cdot T_{\max}$, where $R_{99} = \frac{\log(0.01)}{\log(1-P_s)}$ is the required number of trials to solve a given problem instance (i.e., observe an acceptable solution at least once) with a 99% success rate, and T_{\max} is the estimated physical time required for a single trial at solving a given BoxQP instance on the physical device. In the definition of R_{99} , the quantity P_s denotes the success probability of a single trial; it is found by solving a given problem instance 1000 times and evaluating the number of times the global maximum was found for that given instance. The time for a single trial is estimated as $T_{\max} = n_{\text{iter}} \cdot N \cdot T_{\text{pulse}}$, where T_{pulse} is the time delay between two individual pulses within the cavity; for our benchmarking study, we have used the value $T_{\text{pulse}} = 10$ picoseconds [23]. Figure 1 displays the TTS for finding an approximate solution that is correct up to a multiplicative error. This is because the solutions to the problem instances are intrinsically fractional values, and due to the noise inherent to the method. Figure 1 shows the TTS for different multiplicative factors of the optimal value. For instance, a 0.1% gap indicates that the approximate objective value found is within 0.1% of the global optimal value of the problem. The shaded regions show the interquartile range (IQR), that is, between the 25th and 75th percentiles of the solved problem instances, while the solid curves represent the median. The 75th percentile's edge for the 0.1% gap in the plot for the BMF-CCVM in Fig. 1c goes to infinity, which indicates that approximate solutions with a 0.1% error were found for fewer than 75% of the problem instances. Although the median for the results of the DL-CCVM (Fig. 1a), the MF-CCVM (Fig. 1b), and the PMF-CCVM (Fig. 2f) are similar, the DL-CCVM and the PMF-CCVM dynamics perform better in solving a greater number of the problem instances compared to the MF-CCVM dynamics.

Figure 2 shows the wall-clock TTS (i.e., the TTS for solving the instances on a GPU) for all six solvers introduced in Section II. As shown, the Langevin and pumped Langevin dynamics (Fig. 2a and Fig. 2b, respectively) perform better than the MF-CCVM and the DL-CCVM (Fig. 2d and Fig. 2c, respectively), as the first two involve only one equation per variable, whereas the other two have two equations per variable. This approximately doubles the TTS, as shown in Fig. 2.

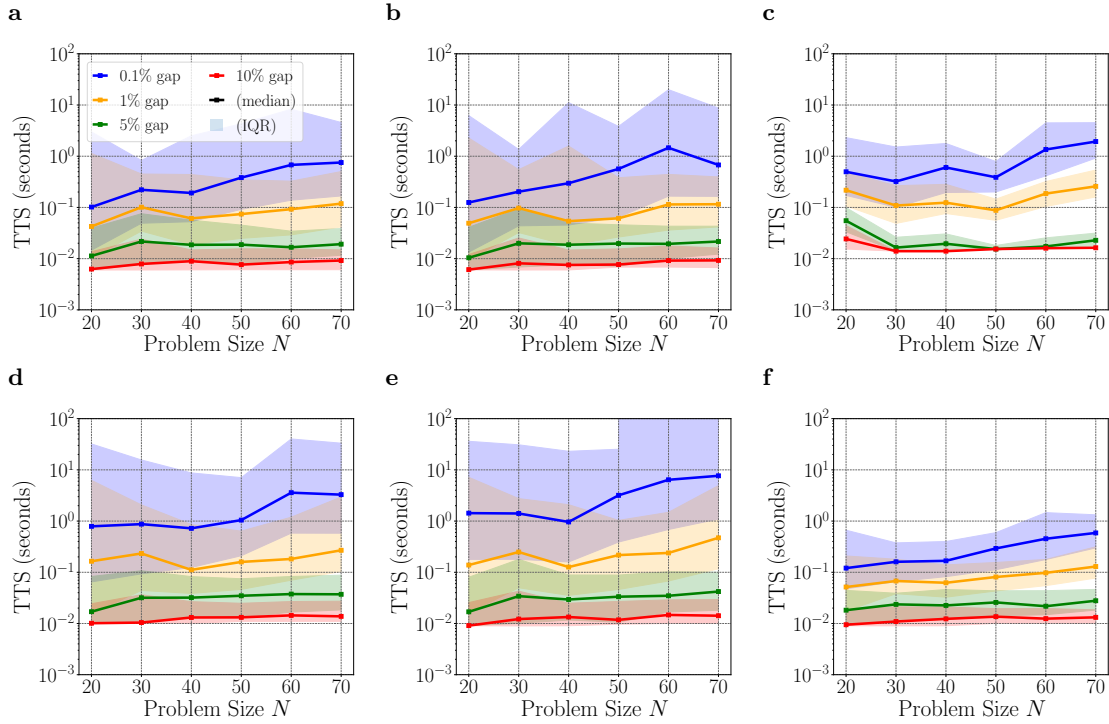


FIG. 2: TTS based on the GPU time for the six solvers defined in Section II: (a) Langevin dynamics, (b) pumped Langevin dynamics, (c) DL-CCVM, (d) MF-CCVM, (e) BMF-CCVM, and (f) PMF-CCVM. For each solver, several TTS curves are displayed, corresponding to finding a solution within a certain target percentage gap from the optimal solution. The shaded regions indicate the IQR for the percentage of instances that were found to be within the specified gap.

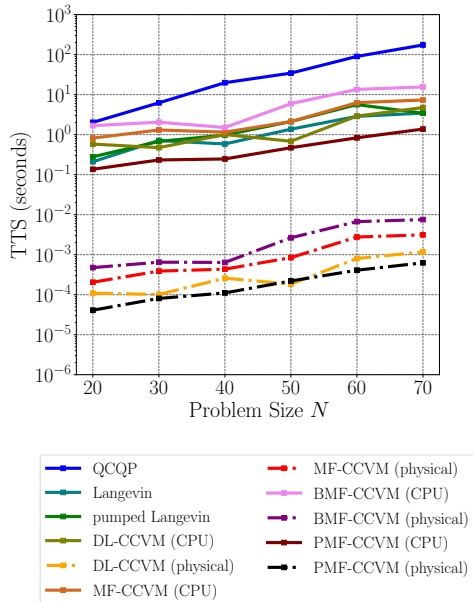


FIG. 3: Wall-clock TTS for optics-based CCVM implementations (dashed-dotted curves) in comparison with the wall-clock TTS for various classical solvers implemented on digital-electronics devices (solid curves). The latter have been computed based on the CPU time, while the former were calculated using the parameters of the corresponding physical device. The estimated TTS values for optics-based CCVM solvers are more than three orders of magnitude lower than the CPU wall-clock TTS values for the digital-electronics based solvers.

Figure 3 shows our benchmarking comparison of the estimated physical TTS for the optics-based implementations of DL-CCVM, MF-CCVM, BMF-CCVM, and PMF-CCVM; the TTS for all six solvers introduced in Section II implemented on digital-electronics devices; and the TTS for the quadratically constrained quadratic programming (QCQP) solver, a general heuristic solver for quadratic programming problems [39]. Optics-based CCVMs can be several orders of magnitude more performant than their electronic counterparts, and, especially in the case of the DL-CCVM, be much more power efficient. Note that, for the PMF-CCVM, the results are similar to those of the Langevin dynamics despite needing to solve the extra equation given for σ_i in Eq. (7). This can be associated with the fact that the PMF-CCVM dynamics [Eq. (7)] and the Langevin dynamics [Eq. (2)] have similar forms.

Figure 4 demonstrates a lack of dependency of the performance of the solvers on the density of Q and V . Specifically, it shows the wall-clock TTS of the six solvers defined in Section II for finding a solution within a 0.1% gap from the optimal solution, individually calculated for various density values of the problem instances. While for exact solvers, such as CPLEX and Gurobi, the TTS heavily depends on the density [37, 38], for the solvers analyzed here, the TTS does not show any significant dependency on it. This is because, unlike the exact solvers, the heuristic solvers analyzed here do not exploit the sparsity of problem instances.

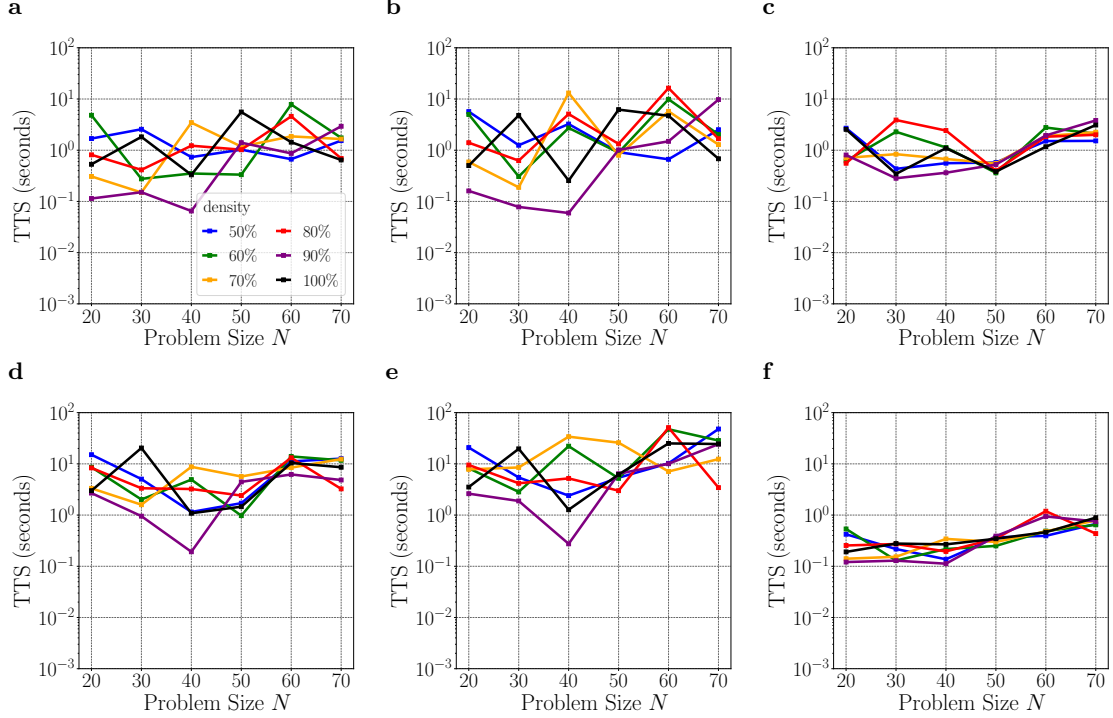


FIG. 4: TTS based on the GPU time for the six solvers defined in Section II, for different densities of the matrix Q and the vector V : (a) Langevin dynamics, (b) pumped Langevin dynamics, (c) DL-CCVM, (d) MF-CCVM, (e) BMF-CCVM, and (f) PMF-CCVM. Solutions within a 0.1% gap of the optimal value were found in all cases. For all solvers, no evident dependency on the density was observed.

V. TIME-EVOLUTION ANALYSIS FOR THE DL-CCVM

Figure 5 shows the time evolution of the DOPO pulses' amplitudes for the DL-CCVM dynamics [Eq. (4)]. A randomly generated problem instance of size $N = 20$ was used for the results displayed in each panel. The heavy dashed lines at -1 and $+1$ indicate the values at which the amplitudes are clamped at the end of the process. The system parameters, including the pump value, are optimized for the highest success probability through parameter tuning. Although the amplitudes do not saturate to -1 and $+1$, these parameters still yield the best performance after the clamping of the amplitudes. Since the clamping is applied at the end of the evolution, it can be considered a post-processing step that is performed on a classical computer. After the clamping of the amplitudes c_i , they are substituted into $x_i = (c_i + 1)/2$ to obtain the problem variables in order to implement the box constraint $0 \leq x_i \leq 1$. It is evident that, for the solutions of the problems, the majority of the variables are found to be at the edges of the box constraint at $x_i = 0$ or $x_i = 1$. For the time evolutions shown in Fig. 5, only one variable has a fractional value within the range $0 < x_i < 1$. The rest of the variables attain the value 0 or 1 in the optimal solution. It is easy to intuitively understand why most variables attain extreme values in BoxQP problems by imagining that, in two dimensions, the chance of a hyperbola's contours touching a corner

of a randomly placed rectangle is much higher than that of becoming tangent to a side of that rectangle.

VI. CONCLUSION

We have proposed an approach for solving problems in the class of NP-hard box-constrained quadratic programming (BoxQP) problems using various modifications to the dynamics of conventional coherent Ising machines (CIM). By exploiting the fact that a CIM operates as a quantum-coherent network of optical pulses with intrinsically continuous amplitudes, the continuous variables of a BoxQP problem can be directly encoded and processed in the CIM natively, without the need to convert them to a binary-variable framework. This allows us to avoid large resource overheads and discretization errors associated with such conversions. Furthermore, the box constraints can be implemented by exploiting the amplitude saturation property of CIMs, or simply by clamping the pulse amplitudes when using a measurement-feedback scheme. Our numerical results motivate operating CIMs or similar coherent-network computing devices as coherent continuous-variable machines (CCVM) in the interest of realizing analog heuristic solvers for non-convex continuous optimization.

Our benchmarking study serves to stimulate research into experimental realizations of the various CCVM schemes proposed in this work, where some of the key

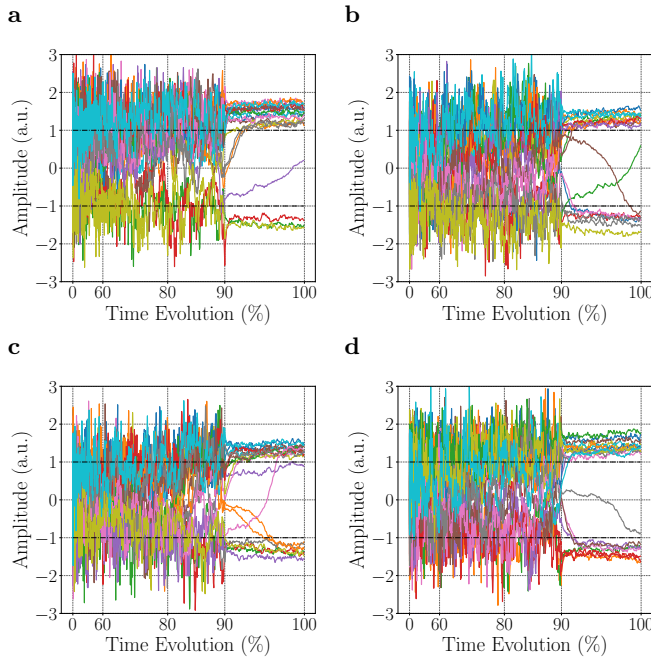


FIG. 5: Time evolution of the DOPO pulses' amplitudes for four randomly generated BoxQP problem instances solved using the DL-CCVM: (a) tuning020-50-2, (b) tuning020-50-3, (c) tuning020-100-0, and (d) tuning020-100-9, where tuning $N-D-S$ indicates a problem instance of size N , density D , and seed number S . The heavy black dashed lines at -1 and $+1$ indicate the values at which the amplitudes are clamped prior to the computation of the objective function. The objective function is calculated after the substitution $x_i = (c_i + 1)/2$ to satisfy the box constraint in Eq. (9), with $l_i = 0$ and $u_i = 1$ for all $i \in \{1, \dots, N\}$. Note that, for each of the problem instances, the majority of the amplitudes have an optimal value at the boundary of the box constraint, while only some of the amplitudes converge to fractional values.

elements present in the conventional CIM architecture may be altered so as to address the requirements of continuous-variable optimization problems. More specifically, our simulations within the BMF-CCVM and PMF-CCVM schemes indicate that the corresponding coherent optical network could effectively solve the BoxQP problem without involving a nonlinear crystal as an active element. In these schemes, the FPGA (or other digital-electronic computing devices), along with the intensity and phase modulators present in the measurement-feedback mechanism, can provide the amplification process required to drive a diffusion process resembling Langevin dynamics. Moreover, as proposed for the PMF-CCVM scheme, an external source (e.g., a laser) may be introduced to compensate for the optical pulse amplitudes' attenuation due to the background photon loss and the loss associated with weak measurements. This may be done in order to keep the drift of the diffusion process close to the gradient of the objective function of the optimization problem, and can be achieved by using the measurement outcomes to dynamically infer and feed the appropriate external pump's field back into the optical cavity. Alternatively, the signal loss can be compensated for directly as part of the measurement-feedback mechanism instead of using another external source. In

deed, the measurement-feedback mechanism can be used to generate the gradient of an arbitrary differentiable objective function serving as the drift term. This is more challenging for CCVM schemes based on optical delay lines, which magnifies the importance of research into the experimental realization of higher-order optical interactions.

ACKNOWLEDGEMENT

The authors thank Yoshihisa Yamamoto, Edwin Ng, Satoshi Kako, and Sam Reifenstein for helpful discussions. We thank our editor, Marko Bucyk, for his careful review and editing of the manuscript. The authors acknowledge the financial support received through the NSF's CIM Expeditions award (CCF-1918549). P. R. acknowledges the financial support of Mike and Ophelia Lazaridis, Innovation, Science and Economic Development Canada (ISED), and the Perimeter Institute for Theoretical Physics. Research at the Perimeter Institute is supported in part by the Government of Canada through ISED and by the Province of Ontario through the Ministry of Colleges and Universities.

[1] S. Burer and A. N. Letchford, Non-convex mixed-integer nonlinear programming: A survey, *Surveys in Operations Research and Management Science* **17**, 97 (2012).

[2] P. Pardalos and G. Schnitger, Checking local optimality in constrained quadratic programming is NP-hard, *Operations Research Letters* **7**, 33 (1988).

[3] S. Burer and D. Vandenbussche, Globally solving box-constrained nonconvex quadratic programs with semidefinite-based finite branch-and-bound, *Computational Optimization and Applications* **43**, 181 (2009).

[4] P. Bonami, O. Günlük, and J. Linderoth, Globally solving nonconvex quadratic programming problems with box constraints via integer programming methods, *Mathematical Programming Computation* **10**, 333 (2018).

[5] S. de Vries and B. Perscheid, Tight compact extended relaxations for nonconvex quadratic programming problems with box constraints, *Journal of Global Optimization* (2022).

[6] N. Mohseni, P. L. McMahon, and T. Byrnes, Ising machines as hardware solvers of combinatorial optimization problems, *Nature Reviews Physics* **4**, 363 (2022).

[7] S. Kirkpatrick, Optimization by simulated annealing, *Science* **220**, 671 (1983).

[8] D. S. Johnson, C. R. Aragon, L. A. McGeoch, and C. Schevon, Optimization by simulated annealing: An experimental evaluation; part I, graph partitioning, *Operations Research* **37**, 865 (1989).

[9] M. Aramon, G. Rosenberg, E. Valiante, T. Miyazawa, H. Tamura, and H. G. Katzgraber, Physics-inspired optimization for quadratic unconstrained problems using a digital annealer, *Frontiers in Physics* **7**, 48 (2019).

[10] T. Takemoto, M. Hayashi, C. Yoshimura, and M. Yamamoto, 2.6 A 2×30 k-spin Multichip Scalable Annealing Processor based on a Processing-In-Memory Approach for Solving Large-Scale Combinatorial Optimization Problems, in *2019 IEEE International Solid-State Circuits Conference-(ISSCC)* (IEEE, 2019) pp. 52–54.

[11] D. de Falco, B. Apolloni, and N. Cesa-Bianchi, A numerical implementation of quantum annealing (1988).

[12] B. Apolloni, C. Carvalho, and D. de Falco, Quantum stochastic optimization, *Stochastic Processes and their Applications* **33**, 233 (1989).

[13] T. Kadowaki and H. Nishimori, Quantum annealing in the transverse Ising model, *Phys. Rev. E* **58**, 5355 (1998).

[14] J. Brooke, D. Bitko, G. Aeppli, *et al.*, Quantum annealing of a disordered magnet, *Science* **284**, 779 (1999).

[15] Z. Wang, A. Marandi, K. Wen, R. L. Byer, and Y. Yamamoto, Coherent Ising machine based on degenerate optical parametric oscillators, *Phys. Rev. A* **88**, 063853 (2013).

[16] Y. Yamamoto, K. Aihara, T. Leleu, K.-i. Kawarabayashi, S. Kako, M. Fejer, K. Inoue, and H. Takesue, Coherent Ising machines—optical neural networks operating at the quantum limit, *npj Quantum Information* **3**, 49 (2017).

[17] U. Benlic, E. K. Burke, and J. R. Woodward, Breakout local search for the multi-objective gate allocation problem, *Computers & Operations Research* **78**, 80 (2017).

[18] V. K. Prajapati, M. Jain, and L. Chouhan, Tabu search algorithm (TSA): A comprehensive survey, in *2020 3rd International Conference on Emerging Technologies in Computer Engineering: Machine Learning and Internet of Things (ICETCE)* (IEEE, 2020) pp. 1–8.

[19] R. Hamerly, T. Inagaki, P. L. McMahon, D. Venturelli, A. Marandi, T. Onodera, E. Ng, C. Langrock, K. Inaba, T. Honjo, *et al.*, Experimental investigation of performance differences between coherent Ising machines and a quantum annealer, *Science Advances* **5**, eaau0823 (2019).

[20] T. Leleu, Y. Yamamoto, P. L. McMahon, and K. Aihara, Destabilization of local minima in analog spin systems by correction of amplitude heterogeneity, *Physical review letters* **122**, 040607 (2019).

[21] T. Leleu, F. Khoyratee, T. Levi, R. Hamerly, T. Kohno, and K. Aihara, Scaling advantage of chaotic amplitude control for high-performance combinatorial optimization, *Communications Physics* **4**, 266 (2021).

[22] S. Reifenstein, S. Kako, F. Khoyratee, T. Leleu, and Y. Yamamoto, Coherent Ising Machines with optical Error Correction Circuits, *Adv. Quantum Technol.* **4**, 2100077 (2021).

[23] K. Sankar, A. Scherer, S. Kako, S. Reifenstein, N. Gherdmarzy, W. B. Krayenhoff, Y. Inui, E. Ng, T. Onodera, P. Ronagh, *et al.*, Benchmark study of quantum algorithms for combinatorial optimization: unitary versus dissipative, *arXiv preprint arXiv:2105.03528* (2021).

[24] K. Takata, A. Marandi, and Y. Yamamoto, Quantum correlation in degenerate optical parametric oscillators with mutual injections, *Phys. Rev. A* **92**, 043821 (2015).

[25] D. Maruo, S. Utsunomiya, and Y. Yamamoto, Truncated Wigner theory of coherent Ising machines based on degenerate optical parametric oscillator network, *Physica Scripta* **91**, 083010 (2016).

[26] S. Kako, T. Leleu, Y. Inui, F. Khoyratee, S. Reifenstein, and Y. Yamamoto, Coherent Ising machines with error correction feedback, *Advanced Quantum Technologies* , 2000045 (2020).

[27] P. L. McMahon, A. Marandi, Y. Haribara, R. Hamerly, C. Langrock, S. Tamate, T. Inagaki, H. Takesue, S. Utsunomiya, K. Aihara, R. L. Byer, M. M. Fejer, H. Mabuchi, and Y. Yamamoto, A fully programmable 100-spin coherent Ising machine with all-to-all connections, *Science* **354**, 614 (2016), <https://www.science.org/doi/pdf/10.1126/science.aah5178>.

[28] Y. Yamamoto, T. Leleu, S. Ganguli, and H. Mabuchi, Coherent Ising machines—quantum optics and neural network perspectives, *Applied Physics Letters* **117**, 160501 (2020), <https://doi.org/10.1063/5.0016140>.

[29] P. Xu, J. Chen, D. Zou, and Q. Gu, Global convergence of Langevin dynamics based algorithms for nonconvex optimization, *arXiv preprint arXiv:1707.06618* (2017).

[30] M. Raginsky, A. Rakhlin, and M. Telgarsky, Non-convex learning via stochastic gradient Langevin dynamics: A nonasymptotic analysis, in *Conference on Learning Theory* (PMLR, 2017) pp. 1674–1703.

[31] P. L. D. Angelis, P. M. Pardalos, and G. Toraldo, Quadratic programming with box constraints, in *Developments in global optimization* (Springer, 1997) pp. 73–93.

[32] K. G. Murty and S. N. Kabadi, *Some NP-complete problems in quadratic and nonlinear programming*, Tech. Rep. (1985).

[33] G. O. Roberts and R. L. Tweedie, Exponential convergence of Langevin distributions and their discrete approx-

imations, Bernoulli (1996).

[34] A. Marandi, Z. Wang, K. Takata, R. L. Byer, and Y. Yamamoto, Network of time-multiplexed optical parametric oscillators as a coherent ising machine, *Nature Photonics* **8**, 937 (2014).

[35] R. Yanagimoto, T. Onodera, E. Ng, L. G. Wright, P. L. McMahon, and H. Mabuchi, Engineering a Kerr-based deterministic cubic phase gate via Gaussian operations, *Physical Review Letters* **124**, 240503 (2020).

[36] T. Shoji, K. Aihara, and Y. Yamamoto, Quantum model for coherent Ising machines: Stochastic differential equations with replicator dynamics, *Phys. Rev. A* **96**, 053833 (2017).

[37] D. Vandenbussche and G. L. Nemhauser, A branch-and-cut algorithm for nonconvex quadratic programs with box constraints, *Mathematical Programming* **102**, 559 (2005).

[38] Gurobi Optimization, LLC, Gurobi Optimizer Reference Manual (2022).

[39] J. Park and S. Boyd, General heuristics for nonconvex quadratically constrained quadratic programming, arXiv preprint arXiv:1703.07870 (2017).